Yasuhiro Iwasawa · Kiyotaka Asakura
Mizuki Tada *Editors*

XAFS Techniques for Catalysts, Nanomaterials, and Surfaces

Springer

XAFS Techniques for Catalysts, Nanomaterials, and Surfaces

Yasuhiro Iwasawa • Kiyotaka Asakura
Mizuki Tada
Editors

XAFS Techniques for Catalysts, Nanomaterials, and Surfaces

Springer

Editors
Yasuhiro Iwasawa
The University of Electro-Communications
Innovation Research Center for Fuel Cells
Graduate School of Informatics and Engineering
Tokyo, Japan

Kiyotaka Asakura
Institute for Catalysis
Hokkaido University
Sapporo, Japan

Emeritus
The University of Tokyo
Tokyo, Japan

Mizuki Tada
Research Center for Materials Science
Nagoya University
Nagoya, Japan

ISBN 978-3-319-43864-1 ISBN 978-3-319-43866-5 (eBook)
DOI 10.1007/978-3-319-43866-5

Library of Congress Control Number: 2016952795

Printed on acid-free paper

This Springer imprint is published by Springer Nature
The registered company is Springer International Publishing AG Switzerland

Preface

This book contains 37 subjects and topics in 5 chapters based on recent developments in the XAFS approach to science and technology, describing the theories, calculation methods, computer programs, advanced methodologies and techniques, experiments, and applications to catalysts, nanoparticles, and surfaces. The book details advanced XAFS techniques and their applications, which enable high-quality research in various areas such as physics, chemistry, materials science, bioscience, engineering, energy science, environmental science, geoscience, metallurgy, and mineralogy. Fundamental characterization of catalysts, nanomaterials, and surfaces is an essential and important area of academic and industrial material development and important to addressing many of today's big global challenges.

The XAFS science and technology has significantly progressed in the past 50 years in association with developments of synchrotron radiation sources and storage rings with lower beam emittance and higher brilliance. In this book we concentrate on the distinct progress, advantage, and merit of the XAFS techniques in conducting fundamental and practical studies on a variety of advanced catalysts, nanomaterials, and surfaces with definite purposes and goals. We also describe recent important issues as examples and future prospects, while also providing the basic theory, principle, and analysis of XAFS and a systematic presentation of relevant data.

Powerful, unique, and versatile, XAFS techniques have provided in situ approaches under working/operando conditions for more realistic molecular-level understanding of catalysis mechanisms and dynamic functions of nanomaterials and surfaces. Recently, XAFS has developed by significant progress in real-time and spatially imaging XAFS measurements. These techniques have provided new pieces of information on real-time structural kinetics and dynamics by real-time characterization and on two- and three-dimensional mapping and visualization of catalyst layers, even a single nanoparticle, sensors, fuel cell electrode catalysts, batteries, biological assemblies, and so on. XAFS analysis methodology has also made progress in applications to more precise characterization of important

catalysts, nanomaterials, and surfaces, which cannot be obtained from other analysis techniques.

This book is written for not only students and academic researchers, but also for people involved in industrial research, in an effort to create synergy between academia, research institutions, and industry. This book is a comprehensive, theoretical, practical, and thorough guide to current XAFS spectroscopy and modern applications involving social needs research. Assuming only undergraduate-level physics, mathematics, and chemistry, the book is ideally suited for graduate students, young scientists, and senior scientists in any disciplines including XAFS-based research. The book also provides guidance to senior undergraduate students for their future research directions and interests.

We were happy to have excellent contributions of many world-class scientists from the USA, the UK, Germany, France, Japan, Italy, the Netherlands, Switzerland, Norway, Brazil, and Russia, reflecting the real international dimension of the book and broad interests and significance of XAFS-based researches. We are pleased to sincerely thank all of them. We thank all Springer staff for continuous encouragement, useful suggestions, and careful production throughout the XAFS book project. We believe that this book can contribute toward present and future fundamental and practical research of the related fields and will satisfy the widest range of researchers and students working in the domain or related topics.

Tokyo, Japan — Yasuhiro Iwasawa
Sapporo, Japan — Kiyotaka Asakura
Nagoya, Japan — Mizuki Tada

Contents

Part I
History and Progress of X-ray Absorption Fine Structure (XAFS)

Chapter 1
History and Progress of X-Ray Absorption Fine Structure (XAFS)

Yasuhiro Iwasawa

The history and progress of X-ray absorption fine structure (XAFS) since the discovery of X-rays (1896), the first theory of X-ray absorption near-edge structure (XANES) (1920), and the first observation and theory of extended X-ray absorption fine structure (EXAFS) (1931) are summarized in Table 1.1, showing principal achievements and landmarks for the theories, calculation methods, computer programs, methodologies and techniques, and applications to catalysts, nanoparticles, and surfaces. Developments of the XAFS approach to science and technology are associated with developments of synchrotron radiation sources and storage rings with increasing brilliance, combined with the production of soft X-rays and particularly hard X-rays, which enable high-quality researches in a variety of scientific fields such as physics, chemistry, bioscience, materials science and engineering, energy science, environmental science, geoscience, metallurgy, mineralogy, etc. Figure 1.1 illustrates the developments of XAFS analyses, measurement cells, frontier methodologies and techniques, spatially and time-resolved applications, and complex-molecular applications, exhibiting their representative examples. Now we find new XAFS paradigms of frontier sciences and technologies for catalysts, nanoparticles, and surfaces, including biomaterials, such as real-time analysis of in situ chemical states, short-lived dynamics, 2D and 3D in situ/operando imaging of real spaces, spatially resolved analysis of inhomogeneous materials, identification of diluted atoms/species, inelastic X-ray scattering analysis at the same chemical sites with different bonding and valence states, in situ analysis under extreme conditions, etc.

XAFS is an *element-specific*, *short-range*, *core-level* X-ray absorption spectroscopy (XAS) with *high sensitivity*. XAFS is divided into two regimes: XANES ($\lesssim$50 eV above around the absorption edge) and EXAFS (over several hundreds

Y. Iwasawa (✉)
Innovation Research Center for Fuel Cells, Graduate School of Informatics and Engineering, The University of Electro-Communications, Chofu, Tokyo 182-8585, Japan
e-mail: iwasawa@pc.uec.ac.jp

Y. Iwasawa et al. (eds.), *XAFS Techniques for Catalysts, Nanomaterials, and Surfaces*, DOI 10.1007/978-3-319-43866-5_1

Table 1.1 The history and progress of XAFS

Year	Theory, simulation, technique, application, etc.	Authors	Published journals
1896	Discovery of X-rays (Nov. 1895)	Röntgen	*Nature* , **53**, 274-277 (1896).
1913	Absorption edge measurement	Broglie	*Comptes Rendus* , **157**, 924-926 (1913).
1920	K-edge absorption	Fricke	*Phys. Rev.* , **16**, 202-215 (1920).
1920	First theory of XANES	Kossel	*Z. Phys.* , **1**, 119-134 (1920).
1931	XAFS for gases at different temperatures	Hanawalt	*Phys. Rev.* , **37**, 715-726 (1931).
1931	First theory of EXAFS	Kronig	*Z. Phys.* , **70**, 317-323 (1931).
1932	Curved crystal transmission spectrograph	Cauchois	*J. Phys. VIII* , **3**, 512-515 (1932).
1954	K-edge absorption	Johnston et al.	*Phys. Rev.* , **94**, 1585-1589 (1954).
1955	Amorphous/crystalline XAS	Sawada et al.	*J. Phys. Soc. Jpn.* , **10**, 464-468 (1955).
1960	K-edge absorption for solid catalysts	Van Nordstrand	*Adv. Catal.* , **12**, 149-187 (1960).
1970	XAFS point scattering theory	Sayers et al.	*Adv. X-ray Anal.* , **13**, 248-271 (1970).
1971	EXAFS Fourier analysis	Sayers et al.	*Phys. Rev. Lett.* , **27**, 1204-1208 (1971).
1972	Amorphou structure by EXAFS	Sayers et al.	*J. Non-Cryst. Solids* , **8-10**, 401-407 (1972).
1972	Total electron yield NEXAFS	Gudat et al.	*Phys. Rev. Lett.* , **29**, 169−172 (1972).
1974	EXAFS measurement at SPEAR	Lytle et al.	*Vacuum ultraviolet radiation physics* , 806-807 (1974).
1974	EXAFS theory	Stern	*Phys. Rev. B* , **10**, 3027-3037 (1974).
1974	Resonant inelastic X-ray scattering	Sparks, Jr.	*Phys. Rev. Lett.* , **33**, 262-265 (1974).
1975	Theory of EXAFS	Pendry et al.	*Phys. Rev. B* , **11**, 2795-2811 (1975).
1975	Total Reflection XRF	Wobrauschek et al.	*Anal. Chem.* , **47**, 852-855 (1975).
1975	XES of water	Nordgren et al.	*J. Phys. B* , **8**, L18-L20 (1975).
1976	Resonant X-ray Raman	Eisenberger et al.	*Phys. Rev. B* , **13**, 2377-2380 (1976).
1976	d band occupancy	Lytle	*J. Catal.* , **43**, 376-379 (1976).
1977	Auger electron yield NEXAFS	Bianconi et al.	*Solid State Commun.* , **24**, 539-542 (1977).
1978	Total electron yield EXAFS	Citrin et al.	*Phys. Rev. Lett.* , **41**, 309-312 (1978).
1978	Surface EXAFS	Stöhr et al.	*Phys. Rev. B* , **18**, 4132-4135 (1978).
1978	Surface EXAFS	Citrin et al.	*Phys. Rev. Lett* ., **41**, 309-312 (1978).
1978	EXAFS of supported Pt catalysts	Sinfelt et al.	*J. Chem. Phys.* , **68**, 2009-2010 (1978).
1979	White line peak intensity	Lytle et al.	*J. Chem. Phys.* , **70**, 4849-4855 (1979).
1980	One-electron XANES interpretation	Hodgson et al.	*J. Chem. Phys.* , **73**, 3274-3288 (1980).
1980	First-principle XANES calculation	Natoli et al.	*Phys. Rev. B* , **22**, 1104-1108 (1980).
1980	DXAFS	Matsushita et al.	*J. Appl. Cryst.* , **13**, 465-471 (1980).
1981	Reflectivity EXAFS	Martens et al.	*J. Phys. C* , **14**, 1523-1534 (1981).
1982	Molecular structure of a supported catalyst	Kuroda et al.	*Chem.Lett.* 1101-1104 (1982).
1982	Multiple scattering XAS calculation	Durham et al.	*Comput. Phys. Commun.* , **25**, 193-205 (1982).
1983	Multiple scattering NEXAFS	Natoli	*EXAFS and near edge structure* , 43-47 (1983).
1984	Multiple scattering XANES experiment	Stern et al.	*Phys. Rev. Lett.* , **52**, 1990-1993 (1984).
1985	In-situ XAFS of Mo_2/SiO_2 catalysis	Iwasawa et al.	*Z. Phys. Chem. N. F.* , **144**, 105-115 (1985).
1986	EXCURVE program	Gurman et al.	*J. Phys. C* , **19**, 1845-1861 (1986).
1986	CONTINUUM program	Natoli et al.	*Phys. Rev. A* , **34**, 4682-4694 (1986).
1986	Dispersive and total reflection XAS	Dartyge et al.	*Phys. Lett.* , **113A**, 384−388 (1986).
1987	X-ray magnetic circular dicroism	Schütz et al.	*Phys. Rev. Lett.* , **58**, 737-740 (1987).
1987	X-ray Raman scattering	Udagawa et al.	*Phys. Rev. B* **36**, 9410-9412 (1987).
1989	Time-resolved QXAFS	Frahm	*Rev. Sci. Instrum.* , **60**, 2515-2518 (1989).
1990	In-situ XAFS of Rh_2/SiO_2 catalysis	Iwasawa et al.	*J. Am. Chem. Soc.* , **112**, 3242-3244, 9096-9104 (1990).
1990	FEFF program	Rehr et al.	*Phys. Rev. B* **41**, 8139-8149 (1990).
1991	High-energy resolution fluorescence detected XANES	Hamalainen et al.	*Phys. Rev. Lett* ., **67**, 2850-2853 (1991).
1992	Polarized total reflection fluorescence EXAFS	Asakura et al.	*Catal. Lett.* , **15**, 247-254 (1992).
1992	Diffraction anomalous fine structure	Stragier et al.	*Phys. Rev. Lett.* , **21**, 3064-3067 (1992).
1993	Diffraction anomalous fine structure	Pickering et al.	*J. Am. Chem. Soc.* , **115**, 6302-6311 (1993).
1993	Laser pump X-ray probe	Thiel et al.	*Nature* , **362**, 40-43 (1993).
1995	Fluorescence μ-XANES	Sutton et al.	*Rev. Sci. Instrum.* , **66**, 1464-1467 (1995).
1995	GNXAS program	Cicco	*Physica B* , **208-209**, 125-128 (1995).
1995	FEFF program	Newville et al.	*Physica B* , **208-209**, 154-156 (1995).
1996	Molecular dynamics (MD)-EXAFS	Fulton et al.	*J. Phys. Chem.*, **100**, 13393-13398 (1996).
1995	EDA program	Kuzmin	*Physica B* , **208-209**, 175-176 (1995).
1997	FDMNES program	Joly	*J. Phys. IV* , **7**, C2-111-115 (1997).
1998	Real space multiple scattering XANES	Rehr et al.	*Phys. Rev. B* , **58**, 7565-7576 (1998).
1998	QXAFS-XRD combination	Clausen	*Catal. Today* , **39**, 293-300 (1998).
1999	Turbo-XAS	Pascarelli et al.	*J. Synchrotron Rad.* , **6**, 1044-1050 (1999).
1999	μ-XANES	Mosbah et al.	*Nucl. Instrum. Methods Phys. Res. Sect. B* , **158**, 214-220 (1999).
1999	Piezo-QEXAFS	Frahm et al.	*J. Synchrotron Rad.* , **6**, 591-593 (1999).
1999	Laser pump X-ray probe	Chen et al.	*J. Phys. Chem. B* , **103**, 3270-3274 (1999).

(continued)

Table 1.1 (continued)

2000	In-situ 1 s time-resolved DXAFS for Cu/ZSM-5 reduction	Yamaguchi et al.	*Catal. Lett.*, **68**, 139-145 (2000).
2000	In-situ 4.7 s time-resolved XAFS for Cu particle change	Böttger et al.	*Chem. Eur. J.*, **6**, 1870-1876 (2000).
2000	SPRKKR	Ebert	*Electr. Struct. & Phys. Prop. Solids*, Springer, 191-246 (2000)
2001	WIEN2k	Schwarz et al.	*Tech. Univ. Wien, Austria*, 2001. ISBN 3-9501031-1-2
2001	IFEFFIT	Newville	*J. Synchrotron Radiat.*, **8**, 322 (2001).
2001	Piezo-QEXAFS	Grunwaldt et al.	*J. Phys. Chem. B*, **105**, 5161-5168 (2001).
2001	Piezo-QEXAFS	Richwin et al.	*J. Synchrotron Rad.*, **8**, 354-356 (2001).
2002	PARATEC	Taillefumier et al.	*Phys. Rev. B*, **66**, 195107(1-8) (2002).
2002	In-situ 30 s time-resolved XANES for oxychlorination catalyst	Lamberti et al.	*Angew. Chem. Int. Ed.*, **41**, 4341-4344 (2002).
2002	15μm μ-XAFS	Fredrickson et al.	*Geochim. Cosmo. Acta*, **66**, 3247-3262 (2002).
2002	180 s time-resolved QXAFS and DXAFS	Dent	*Top. Catal.*, **18**, 2-35 (2003).
2002	μ-fluorescence/tomography	Sutton et al.	Rev. Mineral. & Geochem., **49**, 429-483 (2002).
2003	Reflectivity EXAFS	d'Acapito et al.	*X-ray and Inner-Shell Processes*, 388-394 (2003).
2003	In-situ XAFS for structural kinetics	Iwasawa	*J. Catal.*, **216**, 165-177 (2003).
2003	In-situ 100 ms time-resolved DXAFS for Rh/Al_2O_3 cluster disintegration	Iwasawa et al.	*Angew. Chem. Int. Ed.*, **42**, 4795-4799 (2003).
2003	operando XAFS	Weckhuysen	*Phys. Chem. Chem. Phys.*, **5**, 4351-4360 (2003).
2004	5 μm(KB mirror) μ-XAFS	Paktunc et al.	*Geochim. Cosmo. Acta*, **68**, 969-983 (2004).
2004	0.8 μm(Fresnel zone plate) μ-XAFS	Foriel et al.	*Geochim. Cosmo. Acta*, **68**, 1561-1569 (2004).
2005	ATHENA, ARTEMIS, HEPHAESTUS	Newville et al.	*J. Synchrotron Radiat.*, 12, 537-541 (2005).
2006	Combination of DXANES and XRF for micromapping	Muñoz et al.	*Geochem. Geophys. Geosyst.*, **7**, Q11020(1-10) (2006).
2006	Inelastic X-ray scattering	Fister et al.	*Rev. Sci. Instrum.*, **77**, 063901(1-7) (2006).
2007	In-situ time-resolved time-gating QEXAFS for fuel cells	Tada et al.	*Angew. Chem. Int. Ed.*, **46**, 4310-4315 (2007).
2007	In-situ 2 ms time-resolved DXAFS for oxygen storage/release	Iwasawa et al.	*Angew. Chem. Int. Ed.*, **46**, 9253-9256 (2007).
2007	Galvano QXAFS	Uruga et al.	*AIP Conf. Proc.*, **882**, 914-916 (2007).
2008	Scanning transmission X-ray microscopy	de Groot et al.	*Nature*, 456, 222-225 (2008).
2008	Real-time DFT-XAFS simulation	Vila et al.	*Phys. Rev. B* **78**, 121404(R) (2008).
2009	XANES tomography	Grunwaldt et al.	*Catal. Today*, **145**, 267-278 (2009).
2009	Free electron laser NEXAFS	Bernstein et al.	*Appl. Phys. Lett.*, **95**, 134102(1-3) (2009).
2010	Spatially-resolved QXAFS for CO oxidation	van Bokhoven et al.	*ChemCatChem*, **2**, 653-657 (2010).
2011	Single particle μ-XAFS for $NiO_x/Ce_2Zr_2O_{y\ y}$	Tada et al.	*Phys. Chem. Chem. Phys.*, **13**, 14910-14913 (2011).
2011	In-situ 500 ms time-resolved QXAFS for supported Pd catalyst	Reimann et al.	*J. Am. Chem. Soc.*, **133**, 3921-3930 (2011).
2011	Computed Tomographic XANES	Meirer et al.	*J. Synchrotron Rad.*, **18**, 773-781 (2011).
2011	VUV Fourier-transform spectroscopy	Oliveira et al.	*Nature Photonics*, **5**, 149-153 (2011).
2012	3D Laminography-XAFS for fuel cells	Tada et al. .	*Angew. Chem. Int. Ed.*, **51**, 10311-10314 (2012).
2012	DFT-MD-XAFS	Fulton et al.	*J. Phys. Chem. Lett.*, **3**, 2588-2593 (2012).
2013	Fast scanning microscopic XAFS	Tsuji et al.	*J. Phys.: Conf. Ser.*, **430**, 012019-1-6 (2013).
2014	Intra-nanoparticle nano-XAFS for $Pt/Ce_2Zr_2O_x$	Tada et al.	*ChemPhysChem.*, **15**, 1563-1568 (2014).
2014	Spatially/time-resolved XAFS for zeolite catalysts	Doronkin et al.	*J. Phys. Chem. C*, **118**, 10204–10212 (2014).
2014	Total reflection DXAFS	Abe et al.	*J. Phys.: Conf. Ser.*, **502**, 012035-1-4 (2014).
2014	In-situ 100 ms time-resolved QXAFS for bimetal fuel cells	Tada et al.	*J. Phys. Chem. C*, **118**, 15874-15883 (2014).
2014	2D nano-XAFS imaging for fuel cell degradation	Iwasawa et al.	*Angew. Chem. Int. Ed.* **53**, 14110-14114 (2014).
2014	Back illumination fluorescence XAFS	Asakura et al.	*Phys. Chem. Chem. Phys.*, **16**, 13748-13754 (2014).
2015	Same-view nano-XAFS/STEM-EDS for fuel cell degradation	Iwasawa et al.	*J. Phys. Chem. Lett.* **6**, 2121–2126 (2015).

Discovery and early study
Theories
Calculation methods
Computer programs
Methodologies and techniques
Applications to catalysts, nanoparticles and surfaces

eV after XANES) as shown in Fig. 1.2 (described in Chap. 2 in detail). XANES is associated with the excitation process of a core electron to bound and quasi-bound states, which is especially sensitive to oxidation state (valence) and coordination symmetry of the absorbing atom. EXAFS oscillations are approximately expressed by the sum of the sinusoidal functions of many shells on the basis of single scattering theory involving multiscattering effect by Eq. (1.1), which is usually used as a fitting function.

$$k^n\chi(k) = S_0^2 \sum_{R_i} \frac{k^n N_{R_i} F_{R_i}(k)}{kR_i^2} \sin\left(2kR_i + \Phi_{R_i}(k)\right) \exp\left(-\frac{2R_i}{\lambda_i(k)}\right) \exp\left(-2\sigma_{R_i}^2 k^2\right), \tag{1.1}$$

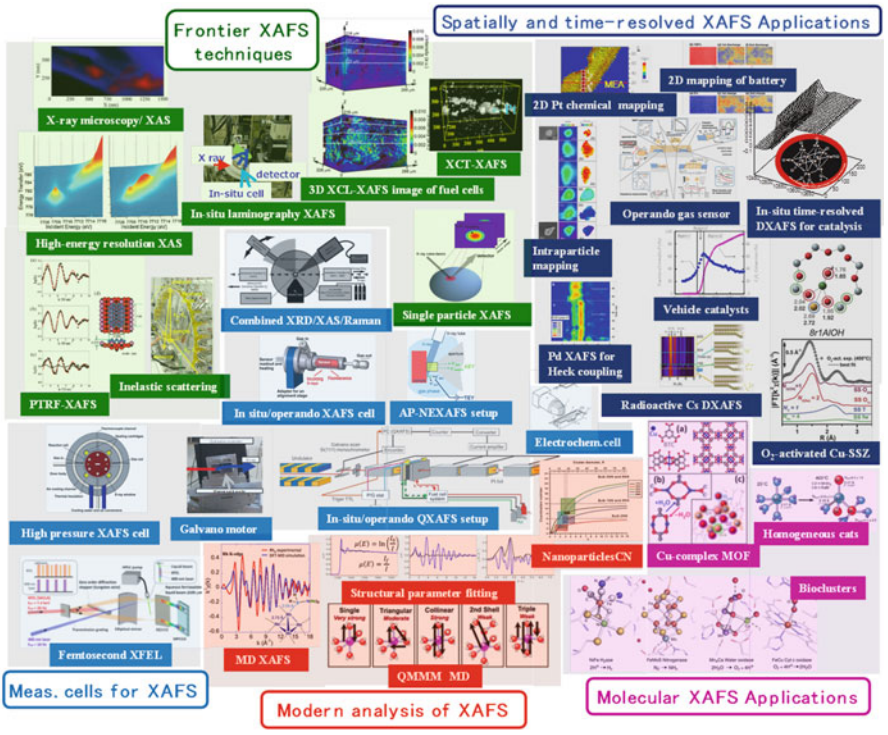

Fig. 1.1 Developments of XAFS: analyses, methods, techniques, and applications

where k, S_0^2, R_i, N, F, ϕ, λ, and σ represent photoelectron wave vector, reduction factor by multiple scattering effect, ith species at distance R, coordination number, back scattering amplitude function, phase shift function, mean free path of photoelectron, and Debye Waller factor, respectively. EXAFS can provide structural information on bond distance, coordination number, and atomic species of the neighbors of the absorbing atom. Thus, XAFS can determine the chemical state and local bonding structure for a selected atomic species. XAFS can be applied to *any sorts of functional materials* such as catalysts, sensors, biomaterials, fuel cells, secondary batteries, electronic devices, optical and magnetic devices, thin films, nano-medicines, etc. without requirement of long-range ordering in structures, *in any atmospheres* such as gas phases, liquids, solids, vacuum, reaction conditions, etc., at low-high temperatures, *for any mixtures and composites*. XAFS has great advantages in deciding molecular-level structures and electronic states of a variety of materials not only in a static state but also in a dynamic state (in situ/operando conditions), which are not possible by other techniques due to their theoretical and experimental analysis limitations.

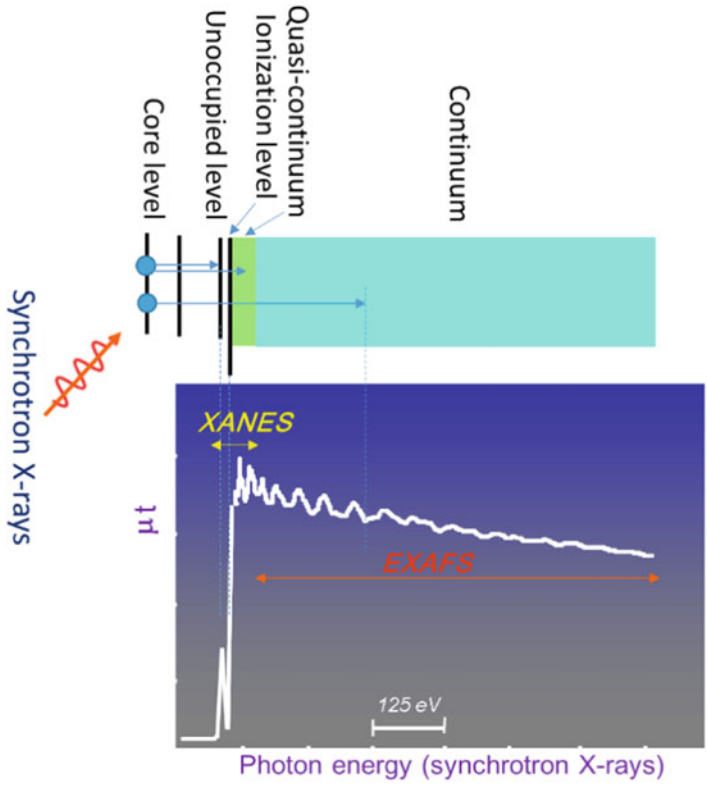

Fig. 1.2 The spectra and origin of XANES and EXAFS

With these advantages as base, the weak points of XAFS are also noted as follows. The XAFS information is one dimensional one averaged over all absorbing atoms with different local structures and environments involved in a sample. The XAFS curve-fitting analysis is not precise in contrast to XRD analysis; e.g., error ranges of bond distance and coordination number are at least ± 0.001 nm and $\pm 10\,\%$, respectively, for most samples of catalysts, nanoparticles, and surfaces. Although the XAFS curve-fitting results involve those error ranges, the XAFS techniques can provide significant structural parameters and electronic states for catalysts, nanoparticles, and surfaces in static and dynamic states, to which other modern physical techniques cannot be applied. Thus, the XAFS techniques have the unique and large advantages enough for scientific discussion on the physical and chemical properties of functional samples, but the XAFS analysis results may be further exactly discussed with the aid of other complementary experiments and theoretical calculations.

XAFS has had a great impact on catalyst research, identifying short-range structures and electronic states of many catalytic systems with nanocrystalline,

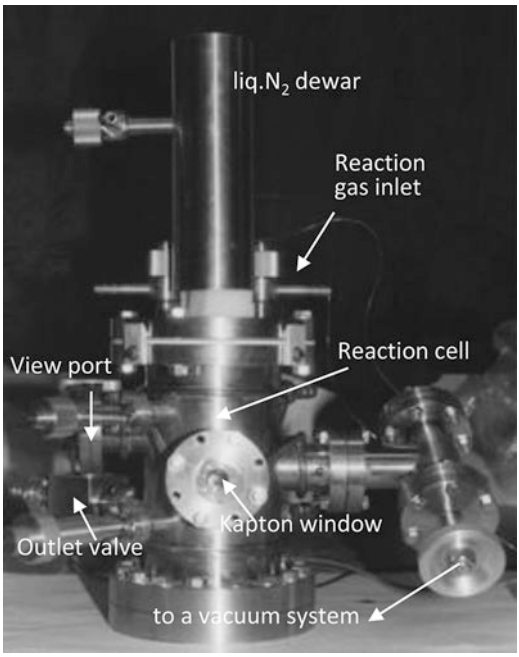

Fig. 1.3 An in-situ XAFS cell for XAFS measurements during catalyst fabrication and catalytic reaction processes

noncrystalline, or disordered phases [1–3]. The essence of catalytic functions and understanding of catalysis may be well characterized by advanced XAFS techniques, which have not been adequately addressed so much [4–6]. Pioneering XAFS works on supported metal catalysts were conducted by Lytle and his coworkers in 1970 years [7–10]. Typically, supported metal particles have usually particle sizes in the range of 1–2 nm diameter without long-range order and hence their structures cannot be targets with XRD. van't Blik et al. studied Rh clusters on Al_2O_3 by EXAFS before and after CO adsorption [11]. They found that the Rh clusters with a Rh-Rh distance of 0.265 nm were disrupted to monomeric Rh atoms bonded to the surface through oxygen after CO adsorption. Sato et al. reported the first molecular structure of a supported catalyst with Mo dimer, determining both metal-metal bonding and metal-light element bonding at the surface [12]. In 1985, Iwasawa et al. reported the first example of in situ characterization of a SiO_2-supported Mo dimer catalyst during the course of selective oxidation of ethanol to acetaldehyde with O_2 using an in situ XAFS cell as shown in Fig. 1.3 [13]. In the in situ XAFS observations the catalyst was treated under the ethanol reaction conditions and quenched by rapid cooling for the observation of key intermediate structures relevant to the catalytic reaction kinetics (see Chap. 21). XAFS has now become routinely used to elucidate the local structures and oxidation states of catalytic materials. XAFS techniques have developed and become essential tools in investigating chemical and physical states of practically real samples with higher

complexity. For example, the electrocatalysis of polymer electrolyte fuel cells (PEFC) for automobiles proceeds at surface layers of small Pt nanoparticles on carbon support in a wet multiphase reaction field under potential-operating PEFC conditions. Recently, the practically real PEFC catalysts were directly measured and visualized by in situ time-resolved XAFS and spatially resolved nano-XAFS imaging techniques to understand and improve the PEFC performance and degradation, whereas they cannot be characterized by other analysis methods, such as XRD, TEM/SEM, SPM, XPS, FT-IR, Raman, ultrafast laser spectroscopies, etc. [14–17].

Finally, science and technology is the wisdom and spirit obtained by humanity through the long history of evolution and is the biggest contributor to the optimization of society. Through the diligent construction of modern science and technology we can build a sustainable society. We have great expectations for advanced XAFS and related techniques for catalysts, nanomaterials, and surfaces in our life and future. The following chapters treat with fundamentals, recent applications, and future prospects of XAFS.

Acknowledgement I thank Dr. Oki Sekizawa at the University of Electro-Communications for his help in listing representative achievements on XAFS research.

References

1. Iwasawa Y (ed) (1996) X-ray absorption fine structure for catalysts and surfaces. World Scientific, Singapore
2. Koningsberger DC, Prins R (1988) X-ray absorption: principles, applications, techniques of EXAFS, SEXAFS and XANES. Wiley, New York
3. Iwasawa Y (1987) Chemical design surfaces for active solid catalysts. Adv Catal 35:187–264
4. Tada M, Zhang S, Malwadkar S, Ishiguro N, Soga J, Nagai Y, Tezuka K, Imoto H, Otsuka-Yao-Matsuo S, Ohkoshi S, Iwasawa Y (2012) The active phase of nickel/ordered $Ce_2Zr_2O_x$ catalysts with a discontinuity ($x = 7–8$) in methane steam reforming. Angew Chem Int Ed 51:9361–9365
5. Tada M, Uruga T, Iwasawa Y (2015) Key factors affecting the performance and durability of cathode electrocatalysts in polymer electrolyte fuel cells characterized by in-situ real time and spatially resolved XAFS techniques. Catal Lett (Silver Anniversary Special Issue) 145:58–70
6. Takao S, Sekizawa O, Samjeské G, Nagamatsu S, Kaneko T, Yamamoto T, Higashi K, Nagasawa K, Uruga T, Iwasawa Y (2015) Same-view nano-XAFS/STEM-EDS imagings of Pt chemical species in Pt/C cathode catalyst layers of a polymer electrolyte fuel cell. J Phys Chem Lett 6:2121–2126
7. Eisenberg P, Kincaid B, Hunter S, Sayers DE, Stern EA, Lytle FW (1974) EXAFS measurements at SPEAR. In: Proc. 4th int. conf. vacuum ultraviolet rad. phys. Pergamon, Oxford, p 806–807
8. Lytle FW (1976) Determination of d-band occupancy in pure metals and supported catalysts by measurement of the L_{III} X-ray absorption threshold. J Catal 43:376–379
9. Sinfelt JH, Via GH, Lytle FW (1978) Extended X-ray absorption fine structure (EXAFS) of supported platinum catalysts. J Chem Phys 68:2009

10. Lytle FW, Wei PSP, Greegor RB, Via GH, Sinfelt JH (1979) Effect of chemical environment on magnitude of x-ray absorption resonance at L_{III} edges. Studies on metallic elements, compounds, and catalysts. J Chem Phys 70:4849
11. van't Blik HFJ, van Zon JBAD, Huizinga T, Vis JC, Koningsberger DC, Prins R (1983) An extended X-ray absorption fine structure spectroscopy study of a highly dispersed. Rh/Al_2O_3 catalyst: the influence of CO chemisorption on the topology of rhodium. J Phys Chem 87:2264–2267
12. Sato Y, Iwasawa Y, Kuroda H (1982) EXAFS study of highly active Mo_2 catalyst. Chem Lett 7:1101–1104
13. Iwasawa Y, Asakura K, Ishii H, Kuroda H (1985) Dynamic behavior of active sites of a SiO_2-attached Mo(VI)-dimer catalyst during ethanol oxidation observed by means of EXAFS. Z Phys Chem N F 144:105–115
14. Tada M, Murata S, Asaoka T, Hiroshima K, Okumura K, Tanida H, Uruga T, Nakanishi H, Matsumoto S, Inada Y, Nomura M, Iwasawa Y (2007) In situ time-resolved dynamic surface events on the Pt/C cathode in a fuel cell under operando conditions. Angew Chem Int Ed 46:4310–4315
15. Saida T, Sekizawa O, Ishiguro N, Uesugi K, Hoshina M, Uruga T, Ohkoshi S, Yokoyama T, Tada M (2012) 4D visualization of a cathode catalyst layer in a polymer electrolyte fuel cell by 3D laminography–XAFS. Angew Chem Int Ed 51:10311–10314
16. Tada M et al (2014) Rate enhancements in structural transformations of Pt-Co and Pt-Ni bimetallic cathode catalysts in polymer electrolyte fuel cells studied by in situ time-resolved X-ray absorption fine structure. J Phys Chem C 118:15874–15883
17. Takao S, Iwasawa Y et al (2014) Mapping platinum species in polymer electrolyte fuel cells by spatially resolved XAFS techniques. Angew Chem Int Ed 53:14110–14114

Part II
Theory and Analysis of XAFS

Chapter 2
Theory and Analysis of XAFS

John J. Rehr, Joshua J. Kas, Fernando D. Vila, and Matthew Newville

2.1 Theory of EXAFS

2.1.1 Introduction

Owing to its element specific and short-range nature, core-level X-ray absorption spectroscopy (XAS) is now routinely used to elucidate the local structural, vibrational, and other physical properties of complex, aperiodic materials. XAS encompasses both extended X-ray absorption fine structure (EXAFS) and X-ray absorption near edge spectra (XANES) [1, 2], where the terms refer, respectively, to the structure in the X-ray absorption spectrum $\mu(\omega)$ at high and low energies relative to the absorption edge with the crossover typically at about 20–30 eV above the edge. The acronym XAFS refers to the fine structure at all energies. The extraordinary capabilities of these spectroscopies come at a price: they depend on comparisons with quantitative simulations of the spectra. Remarkably, however, theories of X-ray spectra have become increasingly accurate and sophisticated, generally overcoming this limitation [2–5].

J.J. Rehr (✉) • J.J. Kas • F.D. Vila
Department of Physics, University of Washington, Seatle, WA, USA
e-mail: jjr@u.washington.edu

M. Newville
University of Chicago, Consortium of Advanced Radiation Sciences, Advanced Photon Source, GSECARS, Argonne, IL, USA
e-mail: newville@cars.uchicago.edu

Y. Iwasawa et al. (eds.), *XAFS Techniques for Catalysts, Nanomaterials, and Surfaces*, DOI 10.1007/978-3-319-43866-5_2

Formally, the theory of XAS is based on Fermi's golden rule

$$\mu(\omega) \sim \sum_F |\langle 0|D|F\rangle|^2 \delta(\omega + E_0 - E_F), \tag{2.1}$$

which requires a summation over exact many-body final states $|F\rangle$, with energies E_F. However, practical calculations depend on the reduction of this relation to an effective, independent particle theory that takes into account several important many-body effects. The theoretical advances in recent years are the result of an improved understanding of these effects and accurate new approximations, in particular for inelastic losses and vibrational damping [6]. These developments rely on physics beyond the usual independent-particle approaches of quantum chemistry and condensed matter such as Hartree–Fock or density functional theory (DFT). Moreover, they involve different limits and time-scales, requiring a variety of approximations and computational methods like Green's function and Lanczos techniques. Besides XAS, these advances are applicable to a number of core-spectroscopies involving electronic excitations, including non-resonant inelastic X-ray scattering (NRIXS, also called X-ray Raman scattering or XRS) [7], and electron energy-loss spectroscopy (EELS) [8–11]. In this chapter we review these advances, focusing on the ideas behind the key approximations needed for a quantitative theory of EXAFS (Sect. 2.1) and XANES (Sect. 2.2). Section 2.3 contains a review of modern XAFS analysis methods, and Sect. 2.4 a number of illustrative structural modeling applications.

2.1.2 The EXAFS Equation

One of the key developments in the history of EXAFS was the famous equation of Sayers, Stern, and Lytle, which represents the normalized fine structure $\chi(\omega) = [\mu(\omega) - \mu_0]/\mu_0$ in XAS in terms of oscillatory contributions from near-neighbor atoms. Here μ_0 is the jump in the XAS at the edge. Although their model was heuristic, it included two key many-body effects, namely the mean free path of the photoelectron and vibrational damping [12]. This key observation demonstrates both the failure of any independent particle interpretation and the need to include both electronic and vibrational effects in quantitative theories. It also shows that XAS is a short-range order phenomenon, and cannot be described using conventional band-structure methods. Remarkably, an exact treatment based on the multiple-scattering (MS) path expansion can be cast in a similar form [1], namely

$$\chi(k) = S_0^2 \sum_R \frac{|f_{\text{eff}}(k)|}{kR^2} \sin(2kR + \Phi_k) e^{-2R/\lambda_k} e^{-2\sigma_R^2 k^2}, \tag{2.2}$$

except that all quantities are redefined to include curved-wave and many-body effects implicitly. In particular f_{eff} is the effective curved wave scattering amplitude

for a given photoelectron wave number k defined relative to the absorption threshold (or Fermi level μ) for X-ray absorption, i.e., with $k^2 = 2(E - \mu)$, λ_k the inelastic mean free path, and σ_R^2 the mean square relative vibrational amplitude of path R. The sum is over all multiple scattering paths, R being the half-path length, S_0^2 the many-body reduction factor which is typically about 0.8 as discussed below, and Φ_k a smoothly varying phase shift. Remarkably, the expansion generally converges rapidly away from the edge, with only of order 10^2 multiple-scattering paths in the EXAFS. This simplification is a consequence of the smallness of λ_k which is generally of order 5–20 Å. This representation also explains why the dominant peaks in the EXAFS Fourier transform $\chi(R) = \mathrm{FT}[\chi(k)]$ are close to the geometrical near-neighbor distances in a material, but shifted by system dependent phase shifts, $\delta R \approx \frac{1}{2} d\Phi_k/dk$. Moreover this MS path representation permits an analysis of experimental XAFS signals in terms of geometrical and vibrational properties of a material, provided one has a reasonable approximation of the phase shifts and λ_k.

2.1.3 Many-Body XAS Formula

Perhaps the easiest way to incorporate many-body effects is to follow the two-step approach derived by Campbell et al. [13]. The first step is the production of the photoelectron, by photoexcitation from a particular core-state, given by an effective one-body (i.e., quasi-particle) absorption $\mu^{(1)}(\omega)$. Second is the effect of inelastic losses and secondary excitations, e.g., plasmons and electron–hole pairs, that can be represented by an energy-dependent "spectral function" $A(\omega, \omega')$, which subsequently broadens and shifts the spectrum. This yields an exact representation of the many-body XAS in terms of a convolution

$$\mu(\omega) = \int d\omega' A(\omega, \omega')\, \mu^{(1)}(\omega - \omega'). \tag{2.3}$$

The shape of the spectral function $A(\omega, \omega')$ typically consists of a sharp "quasi-particle" peak of width related to the inverse mean free path, together with a broad satellite. Consequently the EXAFS problem can be factored into two parts: an effective quasi-particle XAS $\mu^{(1)}(\omega)$ and a part that accounts for inelastic losses. The quasi-particle XAS can be calculated using an independent-particle Fermi's golden rule, with the ΔSCF approximation, i.e., with the final single-particle states $|f\rangle$ calculated with the final state Hamiltonian in the presence of the core-hole

$$\mu^{(1)}(\omega) \sim \sum\nolimits_f |\langle i|d\, P|f\rangle|^2 \delta(\omega + E_i - E_f), \tag{2.4}$$

where $d = \vec{\epsilon} \cdot \vec{r}$ is the dipole operator and P the projection operator onto unoccupied states. Although this is a considerable simplification to Eq. (2.1), the

calculation and summation over final states in the golden rule is a serious computational bottleneck at high energies: the sum can only be carried out efficiently for highly symmetric systems such as atoms, small molecules, or periodic solids. On the other hand, many systems of interest lack symmetry. Reciprocal space (i.e., band structure) methods [14, 15] often ignore the effects of the core-hole and lattice vibrations, which spoil crystal translation symmetry, although the former can be treated approximately with super-cell approximation. Instead, different methods are needed. Remarkably, it is preferable computationally to re-express the XAS in terms of the photoelectron Green's function or propagator G in real space rather than explicitly calculating the final states. This formulation implicitly sums over all final states as can be seen by using the spectral representation of G for which $-\frac{1}{\pi}\mathrm{Im}\,G = \sum_f |f\rangle\,\delta(E-E_f)\,\langle f|$, so that the golden rule can be rewritten exactly as a single matrix element

$$\mu^{(1)}(\omega) = -\frac{1}{\pi}\ \mathrm{Im}\ \langle c|d\ G(r,r',E)\ d'|c\rangle. \tag{2.5}$$

This approach turns out to be advantageous for XAS calculations even in perfect crystals, since inelastic losses (i.e., the mean free path) limit the range probed by XAS experiment to clusters typically of order a few hundred atoms about a given absorption site.

2.1.4 Real-Space Multiple-Scattering Theory

We now briefly summarize the real-space multiple scattering (RSMS) theory used for practical calculations of EXAFS. The starting point of the theory is the separation of the potential into contributions from "scattering potentials" v_R localized on each atomic site R,

$$v_R(r) = v'_{\mathrm{coul}} + \Sigma(E) = \sum\nolimits_R v_R(r-R). \tag{2.6}$$

Here v'_{coul} is the Hartree potential calculated for the final state in the presence of a core hole, and $\Sigma(E)$ is the energy-dependent self-energy. With this separation and the approximation of local spherical symmetry at each site, the propagator is also separable

$$G(r,r',E) = \sum\nolimits_{L,L'} R_L(r) G_{LR,L'R'}\, R_{L'}(r'), \tag{2.7}$$

so that the expression for the XAS can be reduced to a calculation of atomic-like dipole-matrix elements $M_L = \langle c|\epsilon\cdot r|LR\rangle$ and matrix elements of $G(r,r',E)$.

$$\mu(E) = -4\pi e^2 \frac{\omega}{c} \sum_{LL'} M_L(E) G_{LL'} M_{L'}(E), \tag{2.8}$$

where $L = (l, m)$ denotes the angular momentum variables at each site R. Here and elsewhere we interchangeably use either the photoelectron energy E or the photon frequency ω to characterize the photoelectron energy. Interestingly, the relativistic generalization, which is needed for heavy atoms like Pt [16], is identical in form but with relativistic angular momentum variables (k, m). Relativistic corrections are essential for the treatment of spin-orbit effects, which are biggest in the atomic cores and hence crucially important for the transition matrix elements in heavy atoms. However, relativity has only weak effects on scattering of non-relativistic electrons in EXAFS. In FEFF, relativistic effects and spin-orbit corrections are treated to high accuracy using a relativistic Dirac–Fock prescription [17]. In addition the calculation of the scattering potentials at each site simplifies for electrons even of moderate energy (i.e., above about 10 eV of kinetic energy), where the scattering depends strongly on the density in the core of an atom, and hence spherical symmetry is an excellent approximation. Thus, self-consistency is not usually important in calculations of scattering in EXAFS. It is needed, however, to obtain an accurate estimate of the threshold (or Fermi energy E_F) and fractional occupations of the various valence states.

In RSMS, the propagator $G_{LL'}(E)$ naturally separates into intra-atomic contributions from the central atom G_c and multiple scattering contributions from the environment G^{sc}, so that $G = G_c + G^{sc}$. Consequently, the XAS μ naturally factors as

$$\mu(\omega) = \mu_0(\omega)[1 + \chi(\omega)], \tag{2.9}$$

where χ is the X-ray absorption fine structure (XAFS). Thus the net structure in the XAS μ depends both on the atomic background $\mu_0(\omega)$ and on the fine structure χ due to MS: $\chi = \mathrm{Im}\,\mathrm{Tr}_m G^{sc}_{LL'}$. Since $\mu_0(\omega)$ varies weakly with energy, these results are consistent with the experimental definition of the normalized XAFS $\chi = (\mu - \mu_0)/\Delta\mu_0$, where $\Delta\mu_0$ is the jump in the atomic background absorption at threshold. Formally, the matrix $G_{LL'}(E)$ can also be expressed as a sum over all MS paths that a photoelectron can take away from the absorbing atom and back [2], and thus gives rise to the multiple-scattering *path expansion*

$$G^{sc} = e^{i\delta'} \left[G^0 T G^0 + G^0 T G^0 T G^0 + \cdots \right] e^{i\delta}, \tag{2.10}$$

where the successive terms represent single, double, ... scattering processes and δ and δ' are partial-wave phase shifts. As noted above, this expansion converges rapidly for EXAFS with of order 10^2 paths. Remarkably, the sum sometimes converges adequately in XANES, particularly in cases with a short core-hole lifetime as in deep core levels in heavy elements. However, the path expansion is not always reliable near the edge, as discussed in Sect. 2.2. Due to the large dimension of $G_{LR,L'R'}(E)$, exact calculations with the path expansion can only be

carried out for very few low-order MS paths [18]. To overcome this computational bottleneck, an efficient approximation was devised based on the Rehr-Albers (RA) scattering matrix formalism [19]. The RA approach yields curved-wave calculations of the effective scattering amplitude $f_{\rm eff}$ (from which the FEFF code takes its name) in terms of a separable representation of the free propagator $G^0(E)$. With this representation the MS expansion can be re-expressed as a sum over MS paths R in a form essentially the same as the original EXAFS equation of Sayers, Stern, and Lytle [12], but with renormalized ingredients in all terms.

2.1.5 Mean Free Path

Two of the crucial differences between ground state electronic structure and excited states in core-level spectra are (1) the need for an energy dependent self-energy $\Sigma(E)$ instead of an exchange-correlation functional like DFT, and (2) the need for a screened core-hole. The self-energy is essentially a dynamically screened Hartree–Fock exchange interaction, and is the analog of the exchange-correlation potential $V_{\rm xc}$ of DFT. The real part of the self-energy varies by about 10 eV over XAS energies, slowly turning off in the classical limit, while the imaginary part is negative and varies by about 5 eV. The imaginary part accounts for (extrinsic) inelastic losses or final-state broadening, and can be expressed in terms of a mean free path and a core-hole lifetime Γ,

$$\lambda = k/[|\mathrm{Im}\,\Sigma| + \Gamma]. \tag{2.11}$$

The real part of $\Sigma(E)$ accounts for systematic shifts in peak positions compared to those calculated with DFT, leading to a stretching of the energy scale at low energies of about 10 %. One of the key developments in practical XAS codes is an efficient algorithm for calculations of $\Sigma(E)$ based on the GW approximation of Hedin [20]. For example, FEFF and several other XAS codes by default typically use a local density approximation for $\Sigma(E)$ based on the plasmon-pole dielectric constant. This approximation works well for EXAFS, and reduces to the ground state exchange-correlation potential near threshold. However, the plasmon-pole self-energy tends to overestimate losses in the XANES. This deficiency can be overcome by using a many-pole model, as discussed by Kas et al. [21] (see also Sect. 2.2).

2.1.6 Many-Body Amplitude Reduction Factor S_0^2

The effect of the convolution in the exact expression for the XAS in Eq. (2.3) is to average the one-electron XAS over the spectral function, so

$$\mu = \langle \mu_0 \rangle \left[1 + \sum\nolimits_R \langle \chi_R \rangle \right]. \tag{2.12}$$

Since the atomic absorption μ_0 is smoothly varying, the average $\langle \mu_0 \rangle \approx \mu_0$ has little effect. Here $\chi_R \sim \mathrm{Im}\left[\exp(2ikr)\right]$ is the XAFS contribution for a given path. Then, averaging χ_R over the quasi-particle peak gives rise to a damping factor $\exp\left(-2R/\lambda_k\right)$ from the mean free path, while the broad structure in the spectral function gives an additional factor denoted by S_0^2, which turns out to be only weakly dependent on R. Physically the mean free path term is dominated by the extrinsic losses, while S_0^2 is dominated by intrinsic losses. A more detailed analysis shows that this factorization is most appropriate at high energies in the EXAFS regime. Near the edge, one expects interference terms to suppress these effects and hence the energy dependence of these contributions to be important.

2.1.7 Thermal Vibrations and XAFS Debye–Waller Factors

The effects of thermal and structural disorder lead to strong exponential damping of the fine structure, and thus are of crucial importance in XAFS. This damping is dominated by an *XAFS Debye–Waller factor* $\exp\left(-2\sigma^2 k^2\right)$, where σ^2 is the mean square relative displacement (MSRD) of the near-neighbor bonds, and typically varies inversely with the local bond strength. Higher moments of the pair distribution function are sometimes important, especially in temperature dependent investigations of XAS. One of the key theoretical developments in the theory of vibrational damping in XAFS is the cumulant expansion, which yields an efficient parameterization of such thermal and configurational disorder [22, 23] in terms of a few moments or *cumulants* $\sigma^{(n)}$ of the pair distribution function. Formally this expansion yields a complex Debye–Waller factor $\exp\left[\sum_n (2ik)^n \sigma^{(n)}/n!\right]$ in G^{sc}, which contributes both to the amplitude and phase of the XAFS.

The thermal contributions to σ^2 often can be fit to a correlated Debye model [24]. The corrections to the dominant second cumulant depend on anharmonicity. The first cumulant $\sigma^{(1)}$ is the net thermal expansion, while the third $\sigma^{(3)}$ characterizes the asymmetry or skew of the pair distribution function. These odd order contributions can strongly affect the phase of the fine structure, especially at high energy, giving a contribution $2k\sigma^{(1)} - 4k^3\sigma^{(3)}/3 + \cdots$. Relations between the cumulants have been derived [25] which show, to leading order in the anharmonicity parameter, that $\sigma^{(1)} \propto \sigma^2(T)$ and $\sigma^{(3)}$ is related to $\sigma^2(T)$. The third cumulant is important in bond distance determinations and in interpretations of thermal expansion. If the third cumulant is neglected in the analysis, bond distances obtained from EXAFS typically appear unphysically short. Improved treatments of XAFS Debye–Waller factors have recently been developed which go beyond the correlated Debye approximation. They are described in more detail in Sect. 2.4.

2.2 Theory of XANES

2.2.1 Basic Interpretation of XANES

As discussed in the previous section, the formal theories of XANES and EXAFS are essentially the same, and are both given by Fermi's golden rule, i.e., $\mu(\omega) \sim \sum_F |\langle 0|D|F\rangle|^2 \delta(\omega + E_0 - E_F)$, where $|0\rangle$ and $|F\rangle$ are many-body initial and final electronic states. When an effective single-particle description of the spectrum is reasonable, this leads to

$$\mu(\omega) \sim \sum_f |\langle i|d|f\rangle|^2 \delta\big(\omega + \varepsilon_i - \varepsilon_f\big), \tag{2.13}$$

where $|i\rangle$ denotes the core orbital in question, $|f\rangle$ are unoccupied single-particle states, and $d = \vec{\epsilon} \cdot \vec{r}$ is the dipole operator. The basic interpretation of this equation is that the core-level electron is kicked out of the core-level by the photon (dipole transition operator) and into an unoccupied excited state of energy $\varepsilon_f = \varepsilon_c + \omega$, as required by energy conservation. The deep core electrons are very nearly angular momentum eigenstates, e.g., the K-edge is a transition from a 1s orbital. This fact, coupled with the dipole selection rule $l \to l \pm 1$, provides an interpretation of the spectrum in terms of the angular momentum projected density of states (LDOS) and smoothly varying transition matrix elements. For example, transitions from a 1s core-level are related to the p-DOS of the system, while transitions from a 2p core-level are related to the s-DOS and the d-DOS. In many cases the latter dominates and the spectrum can be interpreted in terms of the d-DOS alone. Although the dipole approximation is usually very good, there are some systems for which the pre-edge peaks are due to quadrupole transitions. In this case the selection rules are $\Delta l = 0, \pm 2$, e.g., transitions from the 1s state are related to the s- and d-DOS.

2.2.2 Differences Between XANES and EXAFS

Several of the approximations appropriate for the EXAFS regime (beyond about ~20—30 eV above the edge) are not valid in the near edge regime, with some of these related to the reduction of the many-body formulation to an effective single-particle description, as in Eq. (2.13). For example, in highly correlated systems such as transition metal oxides and f-electron systems, many-body effects can change the qualitative behavior of the near edge spectrum [26], while the main effect on the EXAFS region is simply an overall reduction in the amplitude of the fine structure, which is taken into account by the S_0^2 factor in the EXAFS equation, Eq. (2.2). Even in simpler systems, the approximations made to construct an effective single-particle Hamiltonian, i.e., quasiparticle self-energy models such as the plasmon

pole model, are most appropriate in the EXAFS regime. When calculating XANES they must be augmented, e.g., with the many-pole self-energy model [21]. Another approximation has to do with the description of vibrational and structural distortions. In particular, vibrational effects damp the EXAFS via the Debye–Waller factor $\exp(-2k^2\sigma^2)$. In the XANES, the effects of vibrations and disorder are sometimes more related to symmetry breaking, which allows transitions to states that were previously dipole forbidden, resulting in additional peaks in the near edge spectrum.

EXAFS is also less sensitive to the non-spherical details of the potentials, and a simple overlapped atomic muffin tin potential is adequate for most practical calculations. On the other hand, near-edge spectra can be quite sensitive to details of charge transfer and changes in Fermi level due to solid state effects. Thus the use of self-consistent potentials and often non-spherical symmetry are essential for accurate calculations of XANES. Finally, calculations of the single particle Fermi golden rule must be treated differently in the near edge region because the path expansion detailed in Eq. (2.10) often fails to converge (or converges very slowly) for low energy photoelectrons. This slow convergence is caused by two factors. First, the inelastic mean free path becomes large for low energy electrons so that very long paths must be included in the expansion. Second, large angle scattering amplitudes are not small at low energies, so that the XANES signal is not dominated by nearly linear scattering paths, and all multiple scattering paths must be taken into account.

2.2.3 *Full Multiple Scattering*

Although the path expansion method of calculation is not appropriate for the XANES, one can instead sum the expansion to all orders for any finite cluster of atoms via matrix inversion, so that instead of Eq. (2.10) we have

$$G = \left[1 - G^0 T\right]^{-1} G^0. \tag{2.14}$$

The matrices in this equation are represented in a site and angular momentum basis $|L, R\rangle$, so the rank of the matrix to be inverted is $N(l+1)^2$, where N is the number of atoms in the cluster, and l is the maximum angular momentum of an expansion in spherical harmonics. Matrix inversion can be expensive computationally for large matrices, since the time to invert scales like the cube of the rank of the matrix. Therefore, practical calculations must limit the cluster size and truncate the sum over angular momentum states. The cluster size cannot be too large, typically ~1000 atoms or less for most computations. Fortunately, one does not usually need such large clusters for XANES calculations since the finite core-hole lifetime keeps the inelastic mean free path from becoming too large. In addition, reasonable accuracy requires that $l_{\max}$ is of order $k_{\max}R_{\mathrm{mt}} + l_{\mathrm{occ}}$, where l_{occ} is the largest

angular momentum of the occupied states and $k^2_{\max} \sim E_{\max}$ in Rydberg units. Thus, in the XANES region one can safely set the maximum angular momentum to 4 at most, while at higher energies in the EXAFS matrix inversion becomes impractical. In the intermediate energy regime, Lanczos techniques can be used. In addition, the Green's function $G(E)$ is parameterized by the energy of the photoelectron, thus one inversion must be performed for each energy point in the spectrum. This makes the calculations parallelize naturally and can be done very efficiently on parallel computers [27].

2.2.4 Self-Consistent Potentials

The Green's function can also be used to calculate the total electron density, i.e.,

$$\rho(\vec{r}) = -\frac{1}{\pi}\int_{-\infty}^{\mu} \mathrm{Im}[G(\vec{r},\vec{r},E)]dE. \tag{2.15}$$

Thus the Green's function naturally replaces all the orbitals used in standard density functional theory codes, and the Kohn–Sham Hamiltonian can be solved self-consistently using the Green's function [1]. In the real-space multiple scattering code FEFF, this works as follows:

1. Atomic Dirac–Fock eigenfunctions and densities are calculated for each type of atom, and an overlapped atom approximation to the density is used as the initial guess in the self-consistency loop.
2. The density and exchange correlation functional is used to create a Kohn–Sham (LDA) potential.
3. The spherical muffin-tin approximation is applied.
4. The Green's function is calculated at each energy using a scattering state basis.
5. A new chemical potential μ is found by requiring that the total number of electrons N_e, is conserved, i.e., $N_e = -\frac{1}{\pi}\int_{-\infty}^{\mu}\int d^3r \mathrm{Im}[G(\vec{r},\vec{r},E)]dE$.
6. New densities are calculated from the new Green's function and chemical potential.
7. Steps 2–6 are repeated until the output density is sufficiently close to the input density.

Figure 2.1 shows the structure of the FEFF program, along with details of the self-consistency algorithm. Several other approximations made in FEFF are worth mentioning. First, FEFF allows the user to treat several atoms as identical, even if they are physically different, i.e., two oxygen atoms in different local environments can be constrained to have the same potentials. Second, the integral over space

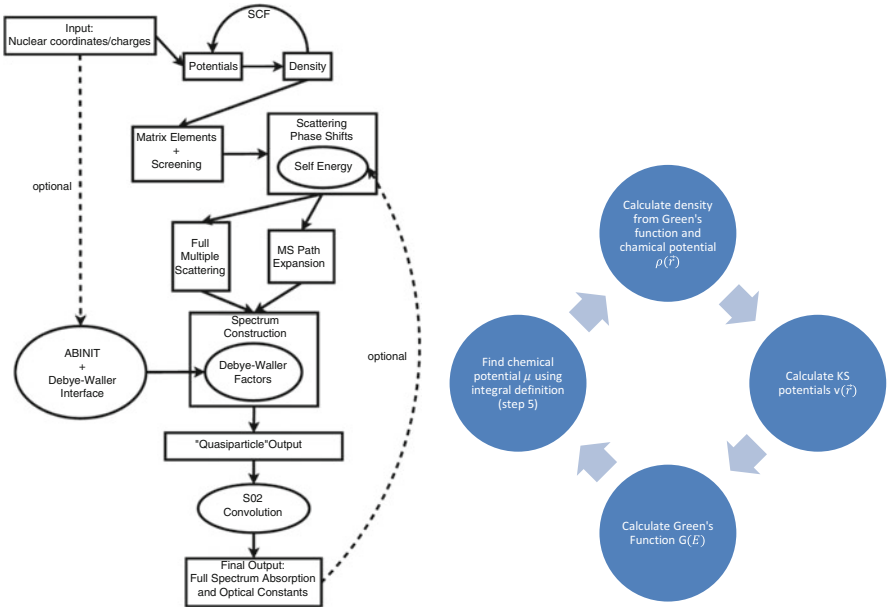

Fig. 2.1 Diagram showing the overall structure of calculations using the FEFF program (*left*) and an expanded view of the SCF procedure (*right*) detailed in the text

shown in step 5 above is approximated by a sum of integrals about each atom. Each of these integrals spans the volume of a sphere (the Norman sphere) defined such that the total overlapped atomic charge (including the nucleus) is zero.

Self-consistency of the densities and potentials can be very important for XANES calculations. For example, if an initial guess of the Fermi energy is too high, pre-edge peaks are missing. Self-consistency and the shift in the Fermi energy due to solid state effects also play a role in chemical shifts, and are very important in systems with multiple, physically unique absorbing sites, such as nanoparticles on a support.

2.2.5 Many-Body Effects: Quasiparticle Self-Energy Models

Many-body effects also play a large role in the XANES, and are responsible for energy dependent shifts and broadenings associated with the quasiparticle self-energy, as well as satellite peaks brought about by multi-electron excitations. While simple models such as the plasmon pole self-energy [28, 29] have been quite successful for calculations of EXAFS, more accurate models must be used near the edge. Most current calculations of these effects are based on the *GW* approximation of Hedin [30], i.e.,